



Cite this: *J. Mater. Chem. C*, 2015, 3, 4039

## The electronic and transport properties of $(VBz)_n@CNT$ and $(VBz)_n@BNNT$ nanocables

Xiu Yan Liang,<sup>a</sup> Guiling Zhang,<sup>\*a</sup> Peng Sun,<sup>a</sup> Yan Shang,<sup>a</sup> Zhao-Di Yang<sup>a</sup> and Xiao Cheng Zeng<sup>\*b</sup>

The electronic structures and transport properties of prototype carbon nanotube (CNT) (10,10) and boron–nitride nanotube (BNNT) (10,10) nanocables, including  $(VBz)_n@CNT$  and  $(VBz)_n@BNNT$  (where Bz =  $C_6H_6$ ), are investigated using the density functional theory (DFT) and the non-equilibrium Green's function (NEGF) methods. It is found that  $(VBz)_n@CNT$  shows a metallic character while  $(VBz)_n@BNNT$  exhibits a half-metallic feature. Both  $(VBz)_n@CNT$  and  $(VBz)_n@BNNT$  nanocables show spin-polarized transport properties, namely, spin-down state gives rise to a higher conductivity than the spin-up state. For  $(VBz)_n@CNT$ , the CNT sheath contributes the metallic transport channel in both spin-up and spin-down states, while the  $(VBz)_n$  core is an effective transport path only in the spin-down state. For  $(VBz)_n@BNNT$ , the BNNT sheath is an insulator in both spin-up and spin-down states. Hence, the transport properties of the  $(VBz)_n@BNNT$  nanocable are attributed to the spin-down state of the  $(VBz)_n$  core. The computed spin filter efficiency of  $(VBz)_n@CNT$  is less than 50% within the bias of  $-1.0$  to  $1.0$  V. In contrast, the spin filter efficiency of  $(VBz)_n@BNNT$  can be greater than 90%, suggesting that the  $(VBz)_n@BNNT$  nanocable is a very good candidate for a spin filter. Moreover, encapsulating  $(VBz)_n$  nanowires into either CNTs or BNNTs can introduce magnetism and the computed Curie or Neél temperatures of both  $(VBz)_n@CNT$  and  $(VBz)_n@BNNT$  are higher than 2000 K. These novel electronic and transport properties of  $(VBz)_n@CNT$  and  $(VBz)_n@BNNT$  nanocables render them as potential nanoparts for nanoelectronic applications.

Received 3rd February 2015,  
Accepted 3rd March 2015

DOI: 10.1039/c5tc00332f

www.rsc.org/MaterialsC

## 1 Introduction

Coaxial nanocables, a novel form of one-dimensional (1D) nanocomposite of a nanowire (NW) (core) enclosed inside a single or multi-wall nanotube (NT) (sheath), have been under much investigation in recent years.<sup>1–5</sup> Various 1D materials with coaxial nanocable-like NW@NT structures have been synthesized in the laboratory, such as  $B@SiO_2$ ,<sup>6</sup>  $SiC@SiO_2$ ,<sup>7</sup>  $TiO_2@SiO_2$ ,<sup>8</sup>  $ZnSe@SiO_2$ ,<sup>9</sup>  $Zn@ZnS$ ,<sup>10</sup> and  $ZnO@ZnS$ .<sup>11</sup> The functionality of nanocables can be broadened compared to that of single-component NWs due to the interplay between NWs and NTs. The combination of the two nanostructures may exhibit new electronic, magnetic, and conducting properties which could offer more prospects and opportunities for applications in nanodevices, magnetic data storage or molecular delivery platforms.<sup>12–19</sup>

Carbon nanotubes (CNTs) and boron nitride nanotubes (BNNTs) are two known 1D hollow nanostructures for accommodating NWs and making nanocables. Various NWs of metals

(Ni, Co, Fe, Cu, Se, Te, Ag),<sup>20–26</sup> polymers (polyaniline, polythiophene),<sup>19,27,28</sup> potassium halide,<sup>29</sup> oxide ( $Fe_3O_4$ ,  $Ga_2O_3$ ),<sup>30–32</sup>  $ZnS$ ,<sup>33</sup> or  $Si$ <sup>34</sup> have already been introduced inside CNTs or BNNTs by using various experimental techniques. Typically, CNTs exhibit delocalized valence bonding character while BNNTs show localized ionic bonding character. So CNTs can be either metallic or semiconducting depending on their diameter and chirality, while BNNTs are insulating regardless of their morphology.<sup>35–40</sup> This difference in electronic properties between CNTs and BNNTs inevitably leads to the different properties of corresponding nanocables. For example, there exists strong coupling between the encapsulated metal (Fe, Co, Ni, or Cu) NW and the CNT, which tends to have substantial modification of the electronic states. In contrast, the interaction between metal NWs and BNNTs is relatively weak and the original electronic structure of NWs is hardly changed by BNNTs.<sup>41–47</sup>

Recently, multidecker organometallic sandwich NWs have attracted growing attention owing to their potential applications in molecular electronic and magnetic devices.<sup>48–57</sup> A number of such multidecker organometallic sandwich NWs have been synthesized.<sup>58,59</sup> In particular, a NW system under intensive investigation is the vanadium–benzene multidecker  $(VBz)_n$  (Bz =  $C_6H_6$ ) NW.<sup>60</sup> The synthesis of  $(VBz)_n$  NWs can be realized from reaction of laser-vaporized metal atoms with

<sup>a</sup> Innovative Research Team of Green Chemical Technology in University of Heilongjiang Province (2014TD007), College of Chemical and Environmental Engineering, Harbin University of Science and Technology, Harbin 150080, China. E-mail: guiling-002@163.com

<sup>b</sup> Department of Chemistry, University of Nebraska-Lincoln, Lincoln, NE 68588, USA. E-mail: xzeng1@unl.edu



$C_6H_6$  in a He atmosphere.<sup>48–49,61</sup> Previous experimental studies have shown that in  $(VBz)_n$  NWs the unpaired electrons on the V atoms are coupled ferromagnetically (FM).<sup>62</sup> Later theoretical studies of  $(VBz)_n$  NWs confirm this FM feature, and also suggest that the ground state of the  $(VBz)_n$  NWs exhibits half metallicity (*i.e.*, one spin channel is metallic while the other spin channel is insulating) and spin filter effect.<sup>63,64</sup> The FM sandwich  $(VBz)_n$  NWs are therefore promising candidates as nanomagnetic building blocks in applications such as recording media or spintronic devices.<sup>65</sup> Other novel sandwich complexes including  $(\eta^5\text{-Cp})FeC_{60}R_5$  ( $R = \text{Me, Ph; Cp} = C_5H_5$ )<sup>66</sup> and ferrocene<sup>67</sup> have also been successfully introduced into CNTs to make a class of self-assembled hybrid structures. We recently showed from *ab initio* calculations that encapsulating  $(C_{60}V)_n$  NWs or ferrocene based molecules into CNTs or BNNTs can result in new physical properties.<sup>68,69</sup> Here, we show that  $(VBz)_n$  NWs can also be introduced into CNTs or BNNTs to form nanocables with multifunctional properties. Particular attention in this study is focused on the electronic and transport properties of  $(VBz)_n@CNT$  and  $(VBz)_n@BNNT$  nanocables as well as the differences in these properties between the nanocables and their CNT, BNNT, and  $(VBz)_n$  components.

## 2 Models and computational methods

Metallic CNTs (10,10) and insulating BNNTs (10,10) are selected as prototype host NTs. For computing electronic structures, the infinite  $(VBz)_n@CNT$  and  $(VBz)_n@BNNT$  systems are modeled using the periodic condition in the axial direction. For computing transport properties, the two-probe devices are adopted. As a benchmark test, we have computed electronic properties based on infinite NT and  $(VBz)_n$  systems and transport properties based on the two-probe devices for pure CNT (10,10), BNNT (10,10), and bare  $(VBz)_n$  systems.

For periodic systems, the supercell contains six layers of the NT (120 atoms) and two units of VBZ [*i.e.*,  $(VBz)_2$ ] inside the NT (Fig. 1) because the lattice parameter of the  $(VBz)_2$  NW ( $\sim 7.38$  Å) nearly matches the lattice parameter of the supercell of CNTs (10,10) and BNNTs (10,10) ( $\sim 7.30$  Å). In addition, such a supercell containing two V atoms can be used to study magnetic coupling between V atoms. The nanocables are separated by 20.0 Å vacuum to neglect tube–tube interaction. All the periodic systems are fully optimized until the maximum absolute force is less than  $0.02$  eV Å<sup>-1</sup>.

For the two-probe devices, we take six optimized unit cells, *i.e.*,  $(VBz)_6@CNT$  or  $(VBz)_6@BNNT$ , as the central scattering region, which is long enough ( $> 21.0$  Å) to separate the left and right electrodes. To compute intrinsic transport properties of the nanocables, we select 1/3 in length of the scattering region as each of the two opposing electrodes (Fig. 1). Transport current is computed by changing the applied bias in steps of 0.2 V in the range of  $-1.0$  to 1.0 V.

All the computations for both infinitely long and two-probe systems are performed using combined DFT/NEGF methods, implemented in the software package Atomistix ToolKit (ATK).<sup>70–73</sup>

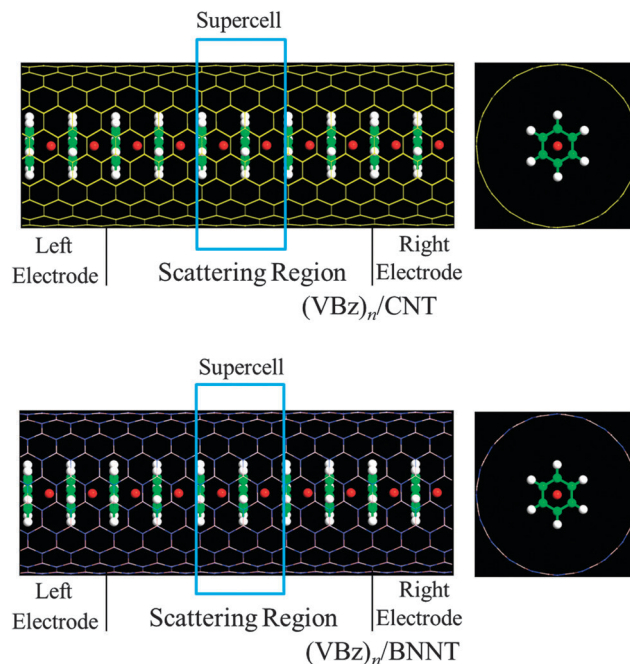


Fig. 1 Optimized structures of  $(VBz)_n@CNT$  and  $(VBz)_n@BNNT$  nanocables, and the two-probe devices for electron transport computation. For the periodic systems, we denote CNT as **1a**,  $(VBz)_n@CNT$  as **1b**, BNNT as **2a**,  $(VBz)_n@BNNT$  as **2b**, and  $(VBz)_n$  as **c**, and for the two-probe devices, we denote CNT as **D-1a**,  $(VBz)_n@CNT$  as **D-1b**, BNNT as **D-2a**,  $(VBz)_n@BNNT$  as **D-2b**, and  $(VBz)_n$  as **D-c**. Color code for the core atoms: V (red); H (white); C (green).

A generalized gradient approximation (GGA) within the Perdew–Burke–Ernzerhof (PBE) formalism is employed to describe the exchange correlations between electrons. The spin polarization of the V atom is considered in all calculations. The on-site correlation effects among the 3d electrons of the V atom are accounted for by using the GGA +  $U$  scheme,<sup>73</sup> where the parameter  $U-J$  is set to be 3.4. A double- $\zeta$  basis with polarization (DZP) is used for all atoms. A  $(1 \times 1 \times 100)$   $k$ -point string in the Brillouin zone ( $x, y, z$  directions, respectively) is adopted, and 150 Ry cutoff energy is applied to describe the periodic wave function. For the sake of simplification, hereafter, we denote CNT as **1a**,  $(VBz)_n@CNT$  as **1b**, BNNT as **2a**,  $(VBz)_n@BNNT$  as **2b**, and  $(VBz)_n$  as **c** for the periodic systems. We also denote CNT as **D-1a**,  $(VBz)_n@CNT$  as **D-1b**, BNNT as **D-2a**,  $(VBz)_n@BNNT$  as **D-2b**, and  $(VBz)_n$  as **D-c** for the two-probe systems.

## 3 Results and discussion

Fig. 1 shows the optimized structures of nanocables  $(VBz)_n@CNT$  and  $(VBz)_n@BNNT$ . First, we show the results of geometry, magnetism, and band structures of the infinitely long nanocables of **1b** and **2b**, followed by transport properties computed based on the two-probe devices of **D-1b** and **D-2b**.

### 3.1 Stability and geometry

Computed total energies per supercell for the optimized **1b** and **2b** are listed in Table 1. The antiferromagnetic (AFM) state and the ferromagnetic (FM) state of the two V atoms are both considered.



Table 1 Calculation results for (VBz)<sub>n</sub>@CNT and (VBz)<sub>n</sub>@BNNT<sup>a</sup>

Species	$E_{\text{Tot,FM}}/\text{eV}$	$E_{\text{Tot,AFM}}/\text{eV}$	$\Delta E_{\text{FM-AFM}}/\text{meV}$	$\Delta E_{\text{r,FM}}/\text{eV}$	$J/\text{meV}$	$T_{\text{C(N)}}/\text{K}$
<b>1b</b>	-24742.12649	-24741.51593	-610.56	-1.060	-610.56	2365.92
<b>2b</b>	-27095.90460	-27095.09389	-810.71	-0.016	-810.71	3133.78

Species	Mulliken population, $P$				Charge, $q/\text{a.u.}$			Magnetic moment, $S/\mu_{\text{B}}$					
	$P_{\text{V}(3\text{d})\uparrow}$	$P_{\text{V}(3\text{d})\downarrow}$	$P_{\text{V}(4\text{s})\uparrow}$	$P_{\text{V}(4\text{s})\downarrow}$	$q_{\text{V}}$	$q_{\text{Bz}}$	$q_{\text{NT}}$	$S_{\text{V}(3\text{d})}$	$S_{\text{V}(4\text{s})}$	$S_{\text{V}}$	$S_{\text{NT}}$	$S_{\text{Bz}}$	$S_{\text{Tot}}$
<b>1b</b>	2.64	0.48	0.05	1.0	0.83	-0.43	-0.4	2.16	-0.95	1.31	0.0	-0.01	1.20
<b>2b</b>	2.71	0.54	0.05	1.0	0.70	-0.72	0.02	2.17	-0.95	1.22	0.0	-0.23	0.99

<sup>a</sup> Computed total energies in the FM or AFM state per supercell ( $E_{\text{Tot,FM}}$ ,  $E_{\text{Tot,AFM}}$ ), the energy difference per supercell between FM and AFM states ( $\Delta E_{\text{FM-AFM}}$ ), the reaction energy per supercell in the FM state ( $\Delta E_{\text{r,FM}}$ ), the exchange parameter per supercell ( $J$ ), the Curie or Néel temperatures ( $T_{\text{C(N)}}$ ), the Mulliken populations of V valence orbitals ( $P_{\text{V}(3\text{d})\uparrow}$ ,  $P_{\text{V}(3\text{d})\downarrow}$ ,  $P_{\text{V}(4\text{s})\uparrow}$ ,  $P_{\text{V}(4\text{s})\downarrow}$ ; the  $\uparrow$  and  $\downarrow$  denote spin-up and spin-down, respectively), the charge distributions on V, Bz, and NT ( $q_{\text{V}}$ ,  $q_{\text{Bz}}$ ,  $q_{\text{NT}}$ ), the local magnetic moments corresponding to the V 3d and 4s states ( $S_{\text{V}(3\text{d})}$  and  $S_{\text{V}(4\text{s})}$ ), the magnetic moment of the V atom ( $S_{\text{V}}$ ), and total magnetic moment per supercell ( $S_{\text{Tot}}$ ).

It is known that pure (VBz)<sub>n</sub> nanowire favors FM ground state.<sup>62,63</sup> Notably, regardless of a CNT or BNNT sheath, the neighboring V atoms of the encapsulated (VBz)<sub>n</sub> still favor the FM coupling as reflected from the lower energy of the FM state compared to the AFM state in both **1b** and **2b**. Hereafter, we mainly focus on the FM state of **1b** and **2b** and discuss associated electronic and transport properties.

The chemical stability of the encapsulated (VBz)<sub>n</sub> is evaluated by computing the reaction energy per supercell for the net reaction  $[\text{NT} + (\text{VBz})_2 \rightarrow (\text{VBz})_2@\text{NT} - \Delta E_{\text{r}}]$  where NT represents the nanotube in a supercell. Here, the computed reaction energies  $\Delta E_{\text{r}}$  are -1.060 and -0.016 eV for **1b** and **2b**, respectively (cf. Table 1). The negative values indicate exothermic reactions. Hence, incorporation of (VBz)<sub>n</sub> into either CNTs or BNNTs is energetically quite favorable.

The optimized supercell length ( $L$ ) in the axial direction, the radii of NTs ( $R$ ), the face-to-face distances between adjacent Bz ( $r_1$ ), the average C-C bond lengths in Bz ( $r_2$ ), and the distances between the H atom of Bz and the nearest atom on NTs ( $r_3$ ) for **1b** and **2b** are given in Table 2. The incorporation of the (VBz)<sub>n</sub> into NTs causes no changes in the supercell length as reflected from the identical values of  $L$  compared to the bare NT. The NT radii  $R$  of **1b** and **2b** are slightly expanded compared with bare **1a** and **2a**, respectively. The distances  $r_1$  are 3.692 Å for both **1b** and **2b**, slightly longer than that (3.40 Å) in pure (VBz)<sub>n</sub>.<sup>74-76</sup> The computed C-C bond lengths in the Bz  $r_2$  range from 1.458 Å to 1.461 Å, very close to the experimentally measured bond length for (VBz)<sub>n</sub> (1.44 Å).<sup>77</sup> The shortest distances between the H atom of Bz and the nearest atom of NTs ( $r_3$ ) are in the range of 4.284–4.456 Å.

Table 2 Computed geometric parameters for (VBz)<sub>n</sub>@CNT and (VBz)<sub>n</sub>@BNNT. The parameters for pure CNT and BNNT are listed for comparison<sup>a</sup>

Species	$L/\text{Å}$	$R/\text{Å}$	$r_1/\text{Å}$	$r_2/\text{Å}$	$r_3/\text{Å}$
Pure CNT <b>1a</b>	7.383	13.568			
(VBz) <sub>n</sub> @CNT <b>1b</b>	7.383	13.799	3.692	1.458	4.284
Pure BNNT <b>2a</b>	7.384	13.669			
(VBz) <sub>n</sub> @BNNT <b>2b</b>	7.384	14.172	3.692	1.461	4.456

<sup>a</sup> The supercell length along the axial direction ( $L$ ), the radii of nanotube ( $R$ ), the face-to-face distances between adjacent Bz ( $r_1$ ), the average C-C bond lengths in Bz ( $r_2$ ), and the distances between H atom of Bz and the nearest atom on nanotube ( $r_3$ ).

### 3.2 Band structures

Fig. 2 displays the computed band structure of **c**, and the corresponding Kohn-Sham orbitals near the Fermi level ( $E_{\text{f}}$ ). It is known that the five 3d orbitals of V atom split into a 3d<sub>z<sup>2</sup></sub> ( $a_1$ ) orbital and two sets of doubly degenerate 3d<sub>xy,x<sup>2</sup>-y<sup>2</sup></sub> ( $e_2$ ) and 3d<sub>xz,yz</sub> ( $e_1$ ) orbitals under the Bz ligand field with  $D_{6h}$  symmetry. Here, the (VBz)<sub>2</sub> supercell contains two V atoms which contribute ten 3d orbitals to couple with the Bz  $\pi$  orbitals, thereby resulting in ten bands:  $a_1'$  and  $a_1''$  bands, two sets of doubly degenerate  $e_2'$  and  $e_2''$  bands, and two sets of doubly degenerate  $e_1'$  and  $e_1''$  bands (cf. Fig. 2). The  $a_1'$  and  $a_1''$  bands are far below the  $E_{\text{f}}$ . In the spin-up state (cf. Fig. 2(a)), the  $e_2''$  and  $e_1'$  bands correspond to the valence and conduction band, respectively, which give a band gap of  $\sim 1.80$  eV, suggesting a semiconducting character. In the spin-down state, the valence  $e_2'$  band and the conduction  $e_1'$  band cross at the  $E_{\text{f}}$  (cf. Fig. 2(b)), showing a metallic character. Thus, the (VBz)<sub>n</sub> NW is indeed a half metal. This result is consistent with experimental observation<sup>62</sup> and other theoretical investigations.<sup>63-65</sup>

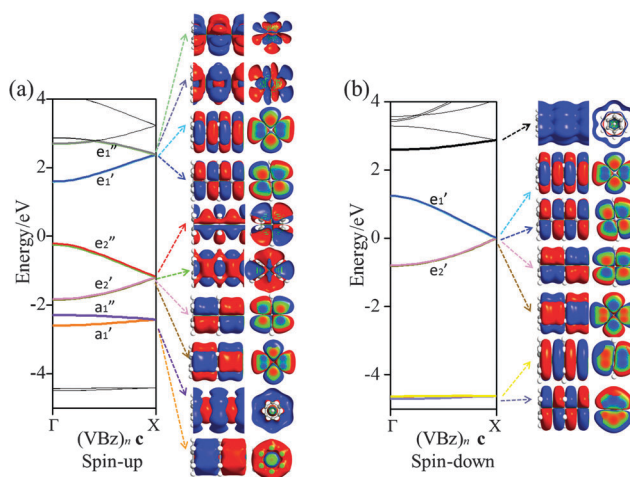


Fig. 2 Computed band structures (left panels) of pure (VBz)<sub>n</sub> and the Kohn-Sham orbitals (middle and right panels) corresponding to the energy levels (highlighted in color lines) near  $E_{\text{f}}$  at the  $\Gamma$  point. The iso-surface value is 0.05 ( $\text{e}^{-3}$ ).



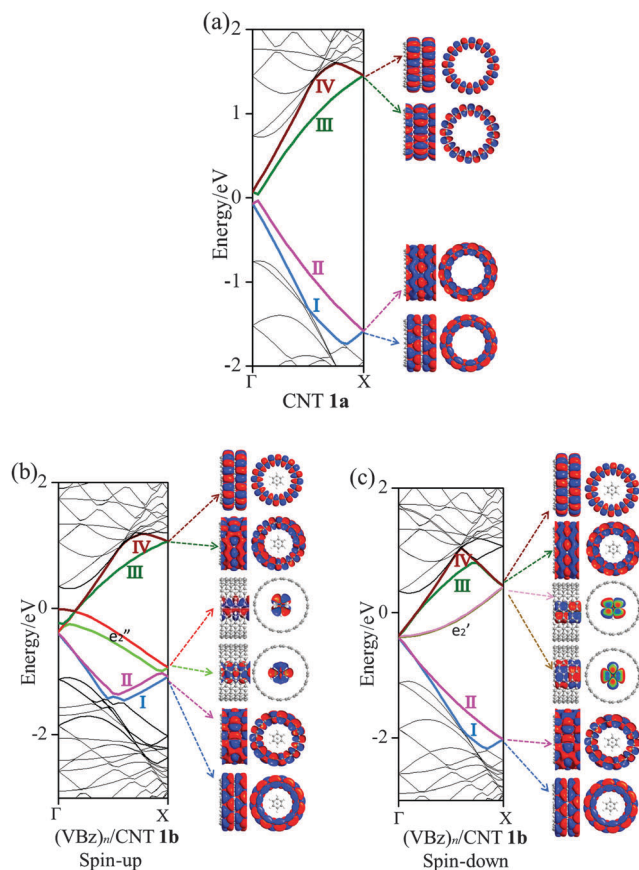


Fig. 3 Computed band structures (left panels) of pure CNT and  $(VBz)_n@CNT$  nanocable and the Kohn–Sham orbitals (middle and right panels) corresponding to the energy levels (highlighted in color lines) near  $E_f$  at the  $\Gamma$  point. The iso-surface value is 0.05 ( $e \text{ \AA}^{-3}$ ).

Fig. 3 displays the computed band structures of **1a** (CNTs) and the nanocable **1b** ( $(VBz)_n@CNT$ ) as well as the corresponding Kohn–Sham orbitals near the Fermi level  $E_f$ . For **1a**, the valence bands I and II and the conduction bands III and IV cross at the  $E_f$  with a large dispersion, reflecting typical metallic characteristics (*cf.* Fig. 3(a)). For **1b**, the spin-up state clearly shows different features from the spin-down state. The unoccupied  $V e'_1$  and  $e'_2$  orbitals are far away from the Fermi level  $E_f$  and thus not plotted in Fig. 3(b) and (c). Compared to **1a**, one can see that the CNT bands III and IV downshift slightly in the spin-up state of **1b** (*cf.* Fig. 3(b)), and both bestride the  $E_f$ . As such, the CNT  $\pi$  state in the spin-up state behaves like partial-filled and should dominate the electron transport. The occupied  $(VBz)_n e'_2$  states are located just below the  $E_f$ , serving as valence bands, and cross with the CNT bands III and IV (*cf.* Fig. 3(b)). The  $(VBz)_n e'_2$  states are mainly originated from  $V 3d_{x^2-y^2}$  states as shown from the plotted Kohn–Sham orbitals. Hence, the V atom can also contribute to the electron transport *via* electron hopping to the CNT sheath. For the spin-down state, the CNT bands III and IV downshift significantly to bestride the  $E_f$  (*cf.* Fig. 3(c)). Thus, the CNT  $\pi$  state in the spin-down state still serves as a major transport pathway. It is noteworthy that the  $(VBz)_n e'_2$  bands upshift significantly to cross the  $E_f$ , serving as a half-filled band. This indicates that the core

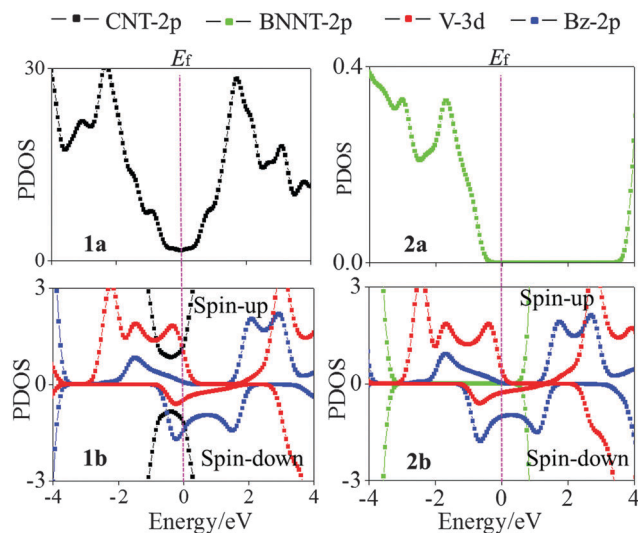


Fig. 4 Computed projected density of states (PDOS) of  $(VBz)_n@CNT$  and  $(VBz)_n@BNNT$  nanocables. For comparison, PDOS of pure CNT and BNNT systems are also presented.

$(VBz)_n$  NW also offers a notable transport pathway along the axial direction. These results can be reflected from the projected density of states (PDOS) as well in Fig. 4. Evidently, the CNT  $\pi$  states of **1a** and **1b** exhibit similar PDOS features, *e.g.*, peaks and broad valleys around the  $E_f$ . Thus, the CNT  $\pi$  states are still the main transport channels even with the core  $(VBz)_n$  NW. For the spin-up state, a similar V–CNT hopping channel arises as the V 3d PDOS peak appears right below the  $E_f$ . For the spin-down state, both the Bz  $\pi$  PDOS and V 3d PDOS cross the  $E_f$  with a half-filled character, again a manifestation of the transport channel along  $(VBz)_n$  NWs. In summary, for nanocable **1b**, both the CNT sheath and the  $(VBz)_n$  core can provide metal-like transport pathways. Moreover, electron hopping from the core  $(VBz)_n$  to the CNT sheath may contribute to electron transport.

In Fig. 5, computed band structures of **2a** (BNNTs) and nanocable **2b** ( $(VBz)_n@BNNT$ ) are plotted along with the associated Kohn–Sham orbitals near the  $E_f$ . For **2a**, as expected, the valence band I is separated from the conduction band II by a large band gap of 4.64 eV (*cf.* Fig. 5(a)). By comparing Fig. 5(b) with 2(a), and Fig. 5(c) with 2(b), we find that the bands originated from the  $(VBz)_n$  NW are little affected even when inside the BNNT. In the spin-up state of **2b**, the  $(VBz)_n a'_1, a'_2, e'_2,$  and  $e'_3$  bands are located between the BNNT band I and the  $E_f$ . The  $(VBz)_n e'_2$  state serves as the valence band and the BNNT  $\pi$  state as the conduction band (*cf.* Fig. 5(b)). As a result, the band gap of **2b** is 1.25 eV, reduced from 4.64 eV of **2a**, showing a semiconducting feature. In the spin-down state, both the valence band  $e'_2$  and the conduction band  $e'_1$  fall in the band gap region of BNNTs and cross at the  $E_f$  just as in the case of **c** (*cf.* Fig. 5(c)). As such, the  $(VBz)_n$  core can offer a metal-like transport path. Overall, encapsulating  $(VBz)_n$  into BNNTs results in the half-metallic properties for **2b**. These properties can be further confirmed from the PDOS in Fig. 4. The BNNT retains the insulating property in **2b** as the BNNT  $\pi$  PDOS are largely separated from the  $E_f$ . In the case of the spin-up state, a



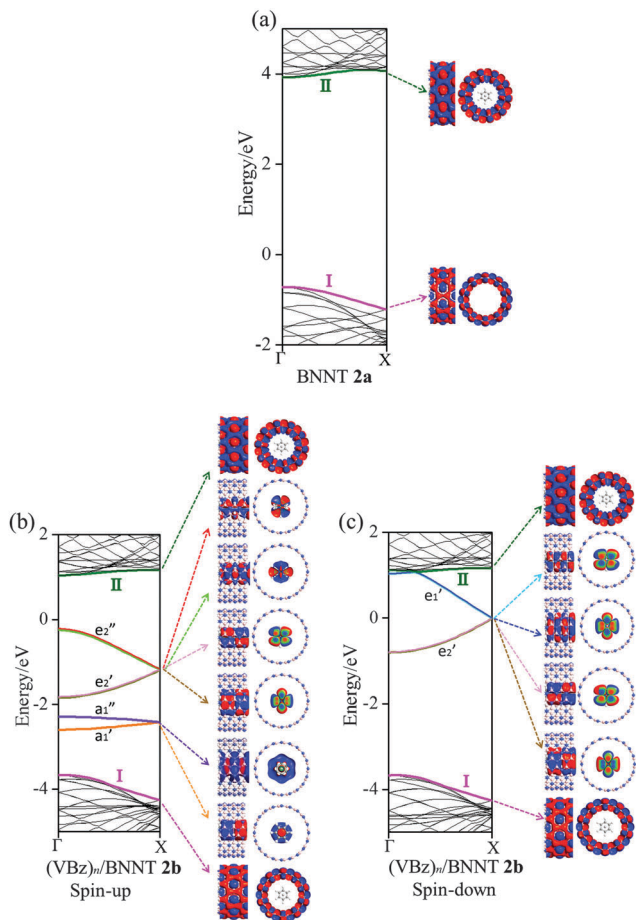


Fig. 5 Computed band structures (left panels) of the pure BNNT and  $(\text{VBz})_n@$ BNNT nanocables and the Kohn–Sham orbitals (middle and right panels) corresponding to the energy levels (highlighted in color lines) near  $E_f$  at the  $\Gamma$  point. The iso-surface value is 0.05 ( $e \text{ \AA}^{-3}$ ).

band gap of about 1.25 eV can be seen between the valence V 3d PDOS and the conduction BNNT  $\pi$  PDOS, showing the semi-conducting character. In the case of the spin-down state, the Bz  $\pi$  PDOS peak is located just across the  $E_f$ , indicating a metallic character. Thus, nanocable **2b** displays a half-metallic character just like pure **c**, different from the metallic character of the nanocable **1b**.

### 3.3 Magnetic properties

As shown in Table 1, both **1b** and **2b** nanocables favor the FM ground state. Table 1 also gives calculated Mulliken population and magnetic moment  $S$  for the FM state of **1b** and **2b**. On one hand, the spin-up V 4s and 3d orbitals donate electrons to the Bz  $\pi$ -orbitals to form coordinate bonds. On the other hand, the Bz  $\pi$ -orbitals feedback electrons to the spin-down V 3d orbital to form feedback bonds. For **1b**, the spin-up V 4s orbital entails only 0.05 electron, *i.e.*, 0.95 electron of the V 4s orbital is transferred to the Bz  $\pi$ -orbital, leading to a negative magnetic moment of  $S_{V(4s)} = -0.95 \mu_B$ . The electron number in the spin-up V 3d orbital decreases to 2.64 from 3.0, *i.e.*, 0.36 electron is transferred to the Bz  $\pi$ -orbitals. Meanwhile, the Bz feedback

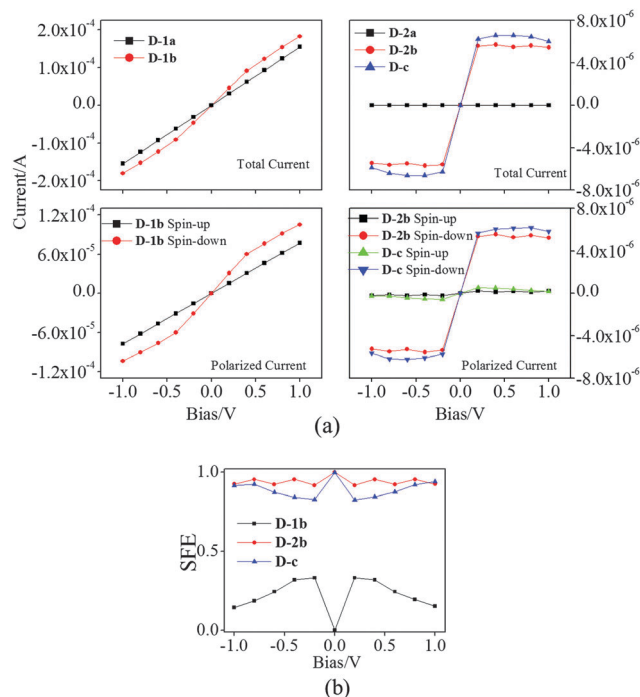


Fig. 6 (a) Computed  $I$ - $V$  curves of two-probe devices of **D-2a** and **D-2b**. For comparison, the  $I$ - $V$  curves for pure CNT **D-1a** and BNNT **D-1b** two-probe devices are also presented. (b) Computed SFE curves under different  $V$  for **D-1b**, **D-2b**, and **D-c** systems.

0.48 electron to the spin-down V 3d orbital. Therefore, the V 3d state generates a positive magnetic moment of  $S_{V(3d)} = 2.16 \mu_B$ . Overall, each V atom in  $(\text{VBz})_n@$ CNT possesses 4.17 valence electrons ( $P_{V(3d)\uparrow} + P_{V(3d)\downarrow} + P_{V(4s)\uparrow} + P_{V(4s)\downarrow}$  in Table 1). The other 0.83 electron from the V atom is distributed over the Bz and the sheath CNT. So the Bz and the CNT bear  $-0.43e$  and  $-0.40e$  charge, respectively.

Notably, as shown in Table 1, CNTs or BNNTs in the nanocable do not show FM behavior as reflected from the zero value of  $S_{\text{NT}}$ . The integer magnetic moment  $S_{\text{Tot}} = 1.20 \mu_B$  for each unit cell  $\text{VBz}@$ CNT mainly arises from the V atom, larger than that for pure **c** ( $S = 1.0 \mu_B$ <sup>64</sup>). In **2b**, the V 4s orbital gives rise to a  $S_{V(4s)} = -0.95 \mu_B$  magnetic moment, while the V 3d orbital induces  $2.17 \mu_B$  magnetic moment, leading to a value of  $S_V = 1.22 \mu_B$  for each V atom in **2b**. The V atom possesses 4.3 valence electrons. Different from **1b**, the donated 0.7 electron from each V in **2b** distributes over the Bz only. The unit cell of BNNTs in **2b** transfers 0.02 electrons to the Bz. These additional electrons given to Bz are partially coupled ferromagnetically, resulting in a magnetic moment of  $S_{\text{Bz}} = -0.23 \mu_B$ . Thus, the integer magnetic moment is reduced to  $0.99 \mu_B$  for each unit cell of **2b**, less than that in **1b** and comparable to that in pure **c**. The exchange parameter  $J$ , which can be estimated by the energy difference between FM and AFM configurations, is about  $-610.56$  meV and  $-810.71$  meV per supercell (containing two V atoms) for **1b** and **2b**, respectively (*cf.* Table 1). The  $J$  value of **2b** is higher than that of **1b**. We also estimate the Curie or Néel temperatures,  $T_{C(N)}$ , of the nanocables using the formula



$3/2k_{\text{B}}T_{\text{C(N)}} = J/2$  (see Table 1). The estimated Curie or Néel temperatures for both **1b** and **2b** are higher than 2000 K, suggesting that the FM state of **1b** and **2b** can be highly stable even at elevated temperatures. The magnetic behavior of **1b** and **2b** nanocables is also reflected by uneven PDOS distribution in the spin-up and spin-down states as shown in Fig. 4. The spin polarization is mainly due to the V atoms.

### 3.4 Transport properties

To analyze the effect of core  $(\text{VBz})_n$  on the transport properties of the two nanocables, we construct a model system such that six unit cells, *i.e.*,  $(\text{VBz})_6@\text{CNT}$  or  $(\text{VBz})_6@\text{BNNT}$ , are

sandwiched between two electrodes, forming a two-probe device as described in Section 2 (*cf.* Fig. 1). Computation results suggest that electric conductivities of the two-probe devices are consistent with the electronic structures of the corresponding infinitely long nanocable systems.

The computed  $I$ - $V$  curves based on the two-probe devices are shown in Fig. 6(a). The magnitude of the total current of pure **D-1a** is on the order of  $10^{-4}$  A, showing good metallic properties, whereas the magnitude of total current of pure **D-c** is two orders of magnitude lower than that of **D-1a**. The conductivity of **D-1a** satisfies Ohm's law, while **D-c** gives a nonlinear  $I$ - $V$  curve in the bias range of  $-1.0$  to  $1.0$  V. Notably, the conductivity is enhanced

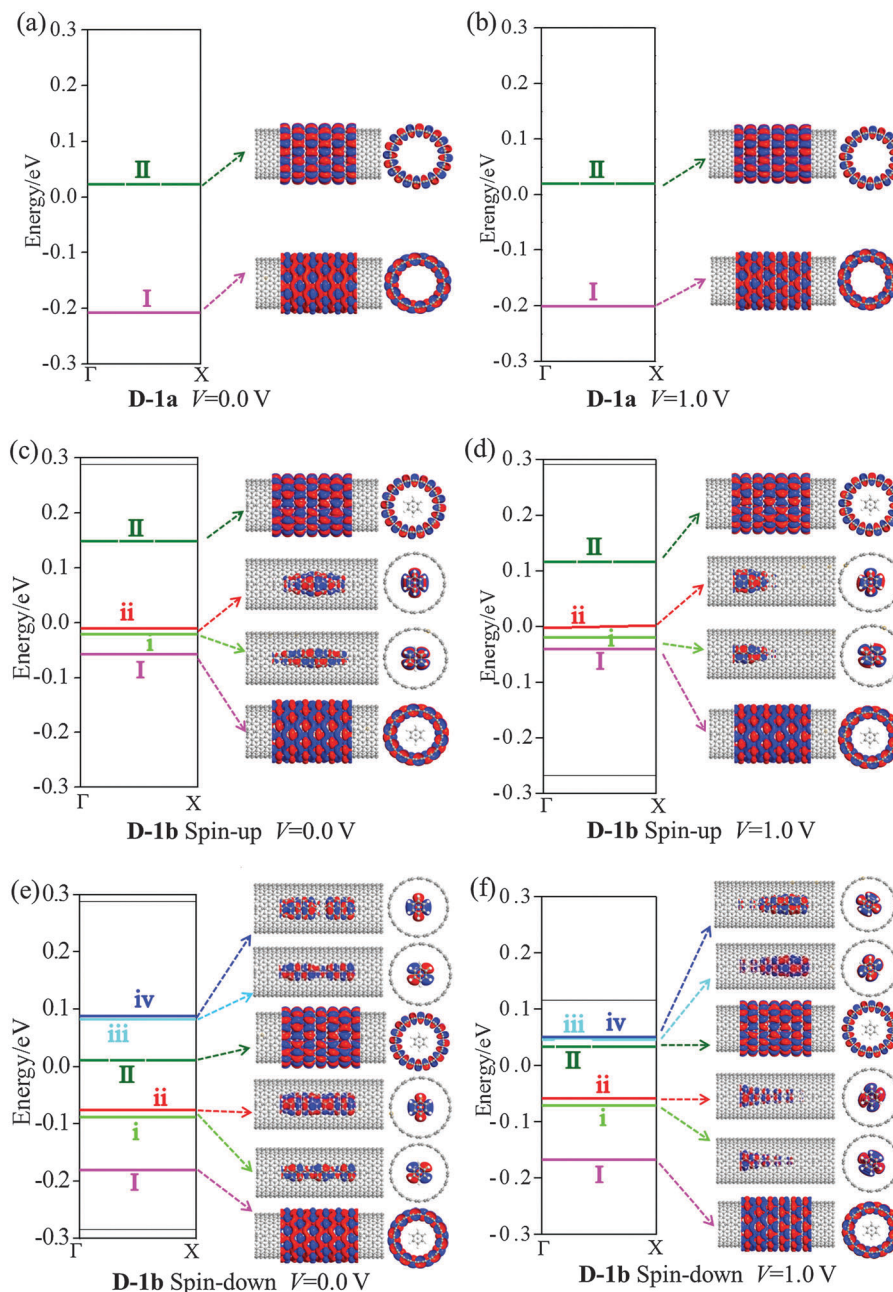


Fig. 7 Computed energy spectra (left panels) of (a), (b) **D-1a** and (c)–(f) **D-1b** two-probe devices. The MPSH states (middle and right panels) correspond to the energy levels (highlighted in color lines) near  $E_{\text{F}}$ . The iso-surface value is  $0.05$  ( $\text{e} \text{ \AA}^{-3}$ ).



when  $(VBz)_n$  is enclosed inside CNTs by comparing the total current of **D-1a** with **D-1b**. This behavior is consistent with the computed electronic structures. Fig. 6(a) shows that pure **D-2a** exhibits features of an insulator with nearly zero current. Clearly, the nanocable **D-2b** displays almost the same conductivity as pure **D-c**, indicating that the  $(VBz)_n$  NW plays the main role in electron transport in **D-2b**, again consistent with computed electronic structures.

For FM **D-1b**, **D-2b**, and **D-c** systems, the spin-up current ( $I_{\uparrow}$ ) and spin-down current ( $I_{\downarrow}$ ) are computed. The conductivities are spin-state dependent within the bias range of  $-1.0$  to  $1.0$  V. The spin-down state gives a higher conductivity than the spin-up state, suggesting that both nanocables and **D-c** can be a spin filter, again consistent with electronic structures of infinitely long **1b**, **2b**, and **c** systems. Another study also indicates that  $(VBz)_n$  coupled to Ni or Co electrodes can be a nearly perfect spin filter.<sup>78</sup>

The spin filter efficiency (SFE) at zero bias voltage can be evaluated from the transmission by using the formula

$$\text{SFE} = \frac{T_{\downarrow}(E_f) - T_{\uparrow}(E_f)}{T_{\downarrow}(E_f) + T_{\uparrow}(E_f)} \quad (1)$$

where  $T_{\downarrow}(E_f)$  and  $T_{\uparrow}(E_f)$  are the transmission coefficients of spin-down and spin-up channel at Fermi energy  $E_f$  under zero bias voltage. At a bias voltage, the SFE is defined as

$$\text{SFE} = \frac{I_{\downarrow} - I_{\uparrow}}{I_{\downarrow} + I_{\uparrow}} \quad (2)$$

where  $I_{\downarrow}$  and  $I_{\uparrow}$  represent spin-down and spin-up current, respectively.

The SFE curves under different bias for **D-1b**, **D-2b**, and **D-c** systems are shown in Fig. 6(b). The SFE values of **D-1b** are all below 50%, whereas **D-2b** gives high values for SFE ( $>90\%$ ). Evidently, the SFE values of **D-2b** are higher than those of **D-c**. So the **D-2b** system exhibits remarkable spin-polarized transport properties, which may be exploited as a new kind of spin filter.

Effects of  $(VBz)_n$  NWs on the transport properties of **D-1b** and **D-2b** can be also analyzed from other aspects such as energy spectra (ES), molecular projected self-consistent Hamiltonian (MPSH) states, transmission spectra (TS), and electrostatic potentials (EP). The results together with those of **D-1a** and **D-2a** are depicted in Fig. 7–10.

Fig. 7 gives the ES and MPSH states for **D-1a** and **D-1b**. For the pure **D-1a**, ES shows little change at  $1.0$  V bias. The HOMO and LUMO (I and II in Fig. 7(a) and (b)) MPSH states of **D-1a** delocalize over the CNT at  $0.0$  and  $1.0$  V bias, indicating that the CNT is an effective transport path. For the spin-up state of **D-1b**, at  $0.0$  V bias, two  $(VBz)_n$  states (i and ii in Fig. 7(c)) appear just below the  $E_f$  and exhibit a delocalized character, in line with the band structures of **1b**. The CNT  $\pi$  states (I and II in Fig. 7(c)) of **D-1b** are nearly the same as those of **D-1a**. The external  $1.0$  V bias exerts little effect on the ES and MPSH states of CNT I and II states of **D-1b** (cf. Fig. 7(d)). However, the MPSH states of i and ii levels of  $(VBz)_n$  shrink considerably and become localized on one side under  $1.0$  V bias. The  $(VBz)_n$  states do not appear above the  $E_f$  within the bias region of  $-1.0$ – $1.0$  V.

The LUMO is mainly dominated by the CNT II state. Therefore, in the spin-up state of **D-1b**, electron transport is still dominated by the CNT. The  $(VBz)_n$  NW in **D-1b** cannot offer an effective transport channel; electron hopping from  $(VBz)_n$  to CNTs may contribute to electron transport.

Fig. 8 shows the TS distribution for **D-1a** and **D-1b**. Like **D-1a**, a flat valley feature can be seen around  $E_f$  at both  $0.0$  and  $1.0$  V bias for the spin-up state of **D-1b**. This again demonstrates that the CNT dominates electron transport in the spin-up state of **D-1b**. For the spin-down state of **D-1b**, the ES, MPSH states, and TS show clearly different characteristics from the spin-up state. At  $0.0$  V bias, four  $(VBz)_n$  states (i–iv in Fig. 7(e)) appear in the energy region of  $-1.0$  to  $1.0$  eV: i and ii are located between  $E_f$  and the CNT I, while iii and iv are located above the CNT II. If  $1.0$  V bias is applied,  $(VBz)_n$  iii and iv levels downshift and come close to the CNT II (cf. Fig. 7(f)). The delocalized feature of the MPSH states of CNT I and II demonstrates high efficiency in electron transport along CNT. The MPSH states of  $(VBz)_n$  i and ii are dispersed over the left side while those of  $(VBz)_n$  iii and iv are scattered over the right side. So electrons can permeate from the left to the right of  $(VBz)_n$ . Thus, in the spin-down state of **D-1b**, the  $(VBz)_n$  NW also behaves as an effective transport path besides the CNT. This is the reason why the spin-down state of **D-1b** exhibits higher conductivity than

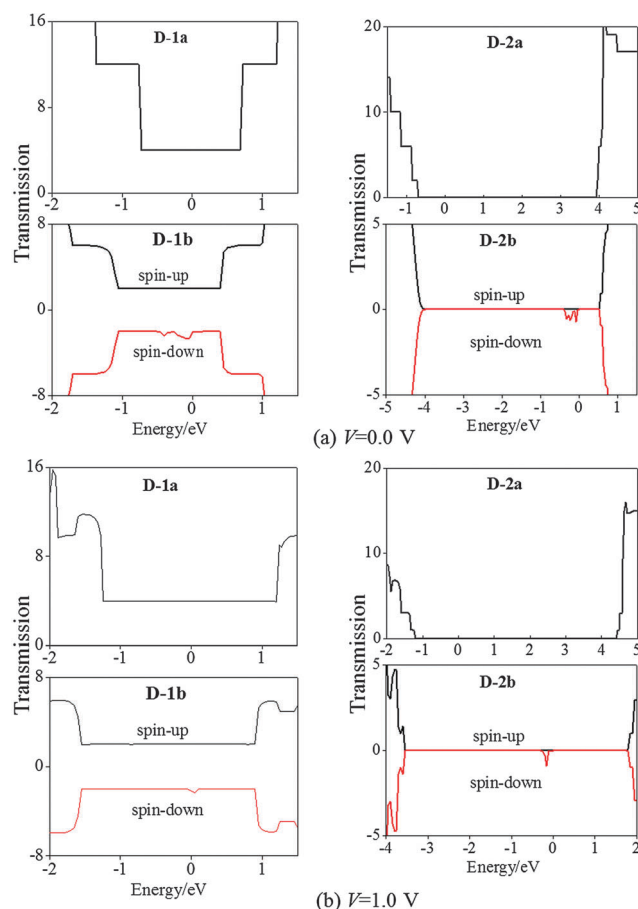


Fig. 8 Transmission spectra (TS) of **D-1a**, **D-1b**, **D-2a**, and **D-2b** two-probe devices.



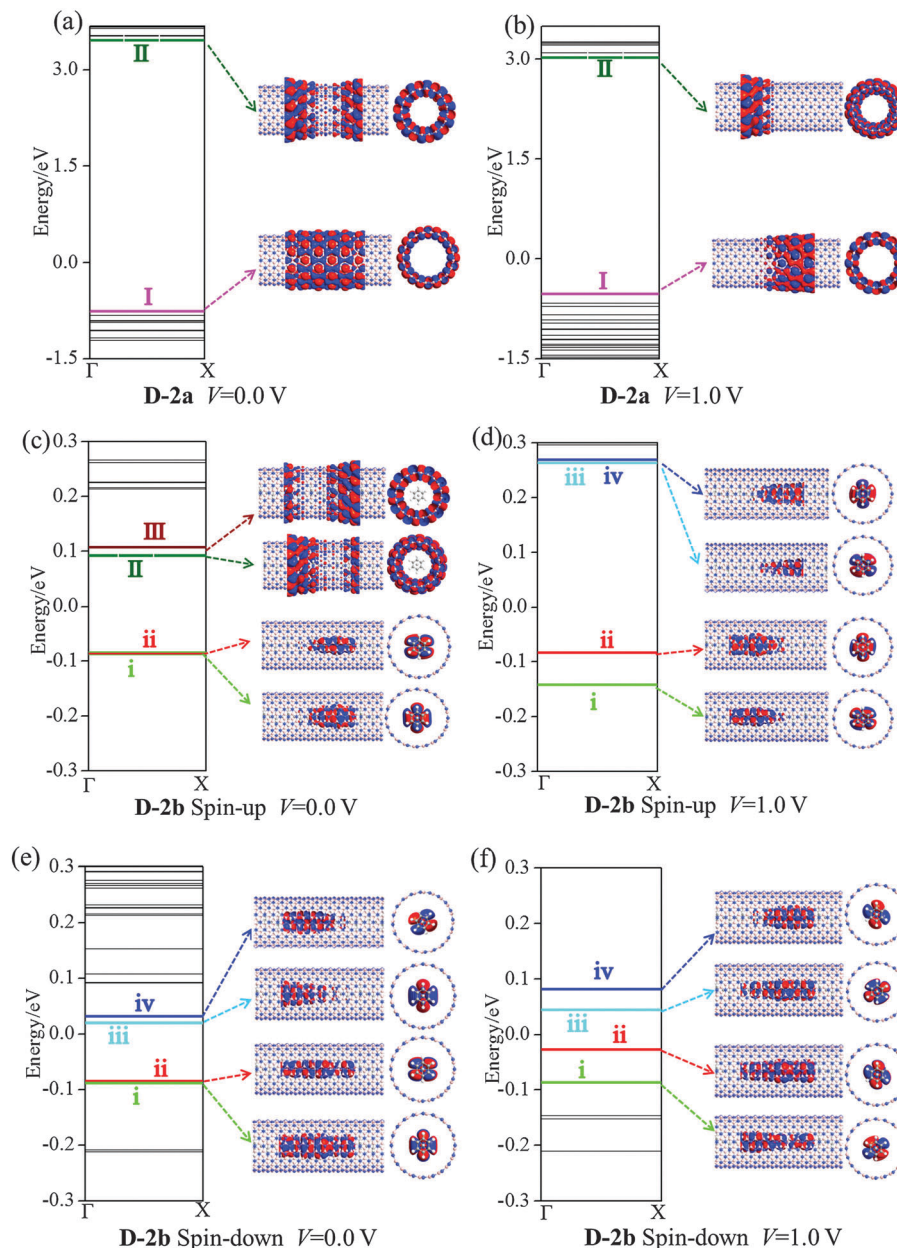


Fig. 9 Computed energy spectra (left panels) of (a), (b) **D-2a** and (c)–(f) **D-2b** two-probe devices and the MPSH states (middle and right panels) corresponding to the energy levels (highlighted in color lines) near  $E_f$ . The iso-surface value is 0.05 ( $e \text{ \AA}^{-3}$ ).

the spin-up state as shown in Fig. 6(a). The TS in Fig. 8 also shows that the spin-down state contributes more peaks around the  $E_f$  than the spin-up state.

Fig. 9 plots the ES and MPSH states at 0.0 and 1.0 V bias for **D-2a** and **D-2b**. The HOMO (I) and LUMO (II) of **D-2a** result in a large energy gap of 4.22 and 3.56 eV at 0.0 and 1.0 V, respectively (Fig. 9(a) and (b)). At 0.0 bias and in the spin-up state of **D-2b**, the  $(VBz)_n$  i and ii states appear below the  $E_f$  and above the BNNT I state (*cf.* Fig. 9(c)). The  $(VBz)_n$  i and ii states turn into the HOMO, and the BNNT II state is still the LUMO in **D-2b**. This is in line with the band structure of periodic **2b**. At 1.0 V bias, the  $(VBz)_n$  states iii and iv are moved toward  $E_f$  and changed into LUMO (*cf.* Fig. 9(d)), that is, both HOMO and

LUMO of the spin-up state of **D-2b** stem from the  $(VBz)_n$  NW under the external bias, giving an energy gap of 0.35 eV. In the case of the spin-down state of **D-2b**, both the HOMO and LUMO are contributed by the  $(VBz)_n$  states regardless of the bias voltage (*cf.* Fig. 9(e) and (f)). Evidently, the HOMO–LUMO gap of spin-down state of **D-2b** is narrowed to 0.07 eV at 0.0 V. This 0.07 eV value is much smaller than that of the spin-up state at 1.0 V (0.35 eV). In addition, the MPSH states of the  $(VBz)_n$  i–iv levels in the spin-down state delocalize more strongly than in the spin-up state, leading to a more effective spin-down transport channel. Hence, the transport properties of **D-2b** are dominated by the spin-down state of the  $(VBz)_n$  NW. Further confirmation can be made through the TS distributions





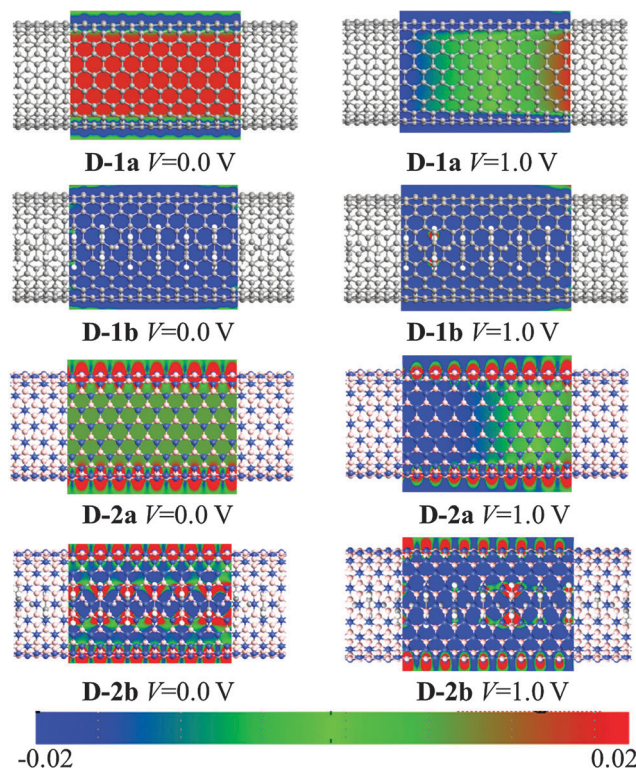


Fig. 10 Computed contour plot of potential distribution for **D-1a**, **D-1b**, **D-2a**, and **D-2b** at 0.0 and 1.0 V. Blue (red) represents low (high) potential.

in Fig. 8. The spin-up state shows no TS contribution both at 0.0 or 1.0 V bias, while the spin-down state shows a peak at the  $E_F$  under both 0.0 and 1.0 V. Thus, **D-2b** displays half-metallic properties arising from the  $(VBz)_n$  NW and should have a high SFE of  $>90\%$ . In contrast, **D-1b** shows a metallic character dominated by CNTs, and thus its SFE is  $<50\%$ .

In addition, we calculate the potential distribution to investigate the barrier in the electron transport along the **D-2a** and **D-2b** by comparing with **D-1a** and **D-1b**. The results are plotted in Fig. 10. Clearly, the CNT serves as an effective transport channel in **D-1a** (blue color). With the  $(VBz)_n$  core, both the CNT and  $(VBz)_n$  act as effective transport paths in **D-1b** as reflected by the blue color of the whole nanocable. In contrast, the BNNT exhibits insulating behavior (red color). The  $(VBz)_n$  core opens a transport pathway for the **D-2b** nanocable.

## 4 Conclusions

We have investigated the electronic and transport properties of a novel form of  $(VBz)_n@CNT$  and  $(VBz)_n@BNNT$  nanocables by means of DFT and NEGF methods. We find that endohedral encapsulation of  $(VBz)_n$  into CNTs (10,10) or BNNTs (10,10) is energetically favorable. Upon encapsulation of  $(VBz)_n$  both  $(VBz)_n@CNT$  and  $(VBz)_n@BNNT$  nanocables exhibit magnetism. More importantly, the ferromagnetic  $(VBz)_n@CNT$  or  $(VBz)_n@BNNT$  is predicted to possess a very high Curie or Neel temperature, all above 2000 K, suggesting a potential candidate as the magnetic nanopart. Conductivities of  $(VBz)_n@CNT$  and

$(VBz)_n@BNNT$  nanocables are dependent on the spin state: the spin-down state gives a higher conductivity than the spin-up state.  $(VBz)_n@CNT$  shows a metallic character while  $(VBz)_n@BNNT$  exhibits half-metallic feature. In the spin-up state of  $(VBz)_n@CNT$ , the electron transport are dominated by the CNT sheath, while the  $(VBz)_n$  core cannot offer an effective transport channel. In the spin-down state of  $(VBz)_n@CNT$ , besides the CNT, the  $(VBz)_n$  core also offers another effective transport pathway. For  $(VBz)_n@BNNT$ , the BNNT is essentially an insulator sheath, while the transport properties of  $(VBz)_n@BNNT$  nanocable are mainly contributed by the spin-down state of the  $(VBz)_n$  core. Values of the spin-filter efficiency of  $(VBz)_n@CNT$  are less than 50%, whereas those of  $(VBz)_n@BNNT$  amount to more than 90%. This suggests that **D-2b** nanocable possesses excellent spin-polarized transport properties, which may be viewed as a new kind of spin filter. Encapsulating  $(VBz)_n$  NWs into either CNTs or BNNTs can effectively tune the electronic and transport properties and both nanocables can be potentially used as functional nanodevices.

## Acknowledgements

GLZ is supported by grants from the NSFC (51073048, 51473042), the SF for leaders in the Academy of Harbin City of China (2013RFXXJ024), and the science foundation for backup leader of leading talent echelon in Heilongjiang province. X CZ is supported by a grant from the US National Science Foundation (NSF) through the Nebraska Materials Research Science and Engineering Center (MRSEC) (grant No. DMR-1420645).

## References

- 1 A. M. Morales and C. M. Lieber, *Science*, 1998, **279**, 208.
- 2 Y. Zhang, K. Suenaga, C. Colliex and S. Iijima, *Science*, 1998, **281**, 973.
- 3 W. S. Shi, H. Y. Peng, L. Xu, N. Wang, Y. Tang and S. T. Lee, *Adv. Mater.*, 2000, **12**, 1927.
- 4 W. Z. Wang, L. Sun, Z. Fang, L. Y. Chen and Z. D. Zhang, *Cryst. Growth Des.*, 2009, **9**, 2117.
- 5 S. J. Guo, J. Li, W. Ren, D. Wen, S. J. Dong and E. K. Wang, *Chem. Mater.*, 2009, **21**, 2247.
- 6 L. M. Cao, H. Tian, Z. Zhang, M. Feng, Z. J. Zhan, W. K. Wang and X. Y. Zhang, *Cryst. Growth Des.*, 2008, **8**, 4350.
- 7 H. F. Zhang, C. M. Wang and L. S. Wang, *Nano Lett.*, 2002, **9**, 941.
- 8 M. Wu, *J. Phys. Chem. C*, 2008, **112**, 13192.
- 9 M. Wang, G. T. Fei, X. G. Zhu, B. Wu and L. D. Zhang, *J. Phys. Chem. C*, 2009, **113**, 8730.
- 10 J. Zhang, F. H. Jiang and Z. H. Dai, *J. Phys. Chem. C*, 2010, **114**, 294.
- 11 C. L. Yan and D. F. Xue, *J. Phys. Chem. B*, 2006, **110**, 25850.
- 12 B. Bouteaux, A. Claye, B. W. Smith, M. Monthieux, D. E. Luzzi and J. E. Fischer, *Chem. Phys. Lett.*, 1999, **310**, 21.
- 13 J. Sloan, R. E. Dunin-Borkowski, J. L. Hutchison, K. S. Coleman, V. C. Williams, J. B. Claridge, A. P. E. York,



- C. Xu, S. R. Bailey, G. Brown, S. Friedrichs and M. L. H. Green, *Chem. Phys. Lett.*, 2000, **316**, 191.
- 14 H. Kataura, Y. Maniwa, T. Kodama, K. Kikuchi, K. Hirahara, K. Suenaga, S. Iijima, S. Suzuki, Y. Achiba and W. Krätschmer, *Synth. Met.*, 2001, **121**, 1195.
- 15 K. Hirahara, S. Bandow, K. Suenaga, H. Kato, T. Okazaki, H. Shinohara and S. Iijima, *Phys. Rev. B: Condens. Matter Mater. Phys.*, 2001, **64**, 115420.
- 16 K. Masatoshi, K. Haruka, S. Takuya, I. Toru, S. Hironori, O. Toshiya, K. Hiromichi, M. Yutaka and Y. Kazuhiro, *J. Am. Chem. Soc.*, 2012, **134**, 9545.
- 17 P. M. Ajayan and S. Iijima, *Nature*, 1993, **361**, 333.
- 18 R. S. Lee, H. J. Kim, J. E. Fischer, A. Thess and R. E. Smalley, *Nature*, 1997, **388**, 255.
- 19 M. Milko, P. Puschnig, P. Blondeau, E. Menna, J. Gao, M. A. Loi and C. Draxl, *J. Phys. Chem. Lett.*, 2013, **4**, 2664.
- 20 K. B. Shelimov and M. Moskovits, *Chem. Mater.*, 2000, **12**, 250.
- 21 D. Golberg, Y. Bando, K. Kurashima and T. Sato, *J. Nanosci. Nanotechnol.*, 2001, **1**, 49.
- 22 C. C. Tang, Y. Bando, D. Golberg, X. X. Ding and S. R. Qi, *J. Phys. Chem. B*, 2003, **107**, 6539.
- 23 R. Z. Ma, Y. Bando and T. Sato, *Chem. Phys. Lett.*, 2004, **350**, 1.
- 24 A. L. M. Reddy, B. K. Gupta, T. N. Narayanan, A. A. Martí, P. M. Ajayan and G. C. Walker, *J. Phys. Chem. C*, 2012, **116**, 12803.
- 25 O. E. D. Rodrigues, G. D. Saraiva, R. O. Nascimento, E. B. Barros, F. J. Mendes, Y. A. Kim, M. Endo, M. Terrones, M. S. Dresselhaus and F. A. G. Souza, *Nano Lett.*, 2008, **8**, 3651.
- 26 G. C. Xi, C. Wang, X. Wang, Y. T. Qian and H. Q. Xiao, *J. Phys. Chem. C*, 2008, **112**, 965.
- 27 Y. Takashi and Y. Hiroki, *J. Phys. Chem. C*, 2014, **118**, 5510.
- 28 G. Pietro, B. Andrea, C. Matteo and Z. Francesco, *J. Phys. Chem. C*, 2014, **118**, 5032.
- 29 W. Q. Han, C. W. Chang and A. Zettl, *Nano Lett.*, 2004, **4**, 1355.
- 30 H. Jiang, Y. Hu, S. Guo, C. Yan, P. S. Lee and C. Li, *ACS Nano*, 2014, **8**, 6038.
- 31 R. Z. Ma, Y. Bando and T. Sato, *Adv. Mater.*, 2002, **14**, 366.
- 32 H. S. Song, J. Zhang, J. Lin, S. J. Liu, J. J. Lou, Y. Huang, E. M. Elssfah, A. Elsanousi, X. X. Ding, J. M. Gao and C. Tang, *J. Phys. Chem. C*, 2007, **111**, 1136.
- 33 D. C. Wei, Y. Q. Liu, L. C. Cao, H. L. Zhang, L. P. Huang and G. Yu, *Chem. Mater.*, 2010, **22**, 288.
- 34 B. Wang, X. L. Li, X. F. Zhang, B. Luo, M. H. Jin, M. H. Liang, A. D. S. T. Shadi and L. J. Zhi, *ACS Nano*, 2013, **7**, 1437.
- 35 A. Rubio, J. L. Corkill and M. L. Cohen, *Phys. Rev. B: Condens. Matter Mater. Phys.*, 1994, **49**, 5081.
- 36 N. G. Chopra, R. J. Luyken, K. Cherrey, V. H. Crespi, M. L. Cohen, S. G. Louie and A. Zettl, *Science*, 1995, **269**, 966.
- 37 E. Hernandez, C. Goze, P. Bernier and A. Rubio, *Phys. Rev. Lett.*, 1998, **80**, 4502.
- 38 C. W. Chang, A. M. Fennimore, A. Afanasiev, D. Okawa, T. Ikuno, H. Garcia, L. Deyu, A. Majumdar and A. Zettl, *Phys. Rev. Lett.*, 2006, **97**, 085901.
- 39 D. Golberg, X. D. Bai, M. Mitome, C. C. Tang, C. Y. Zhi and Y. Bando, *Acta Mater.*, 2007, **55**, 1293.
- 40 Y. Chen, J. Zhou, S. J. Campbell and G. L. Caer, *Appl. Phys. Lett.*, 2004, **84**, 2430.
- 41 K. B. Shelimov and M. Moskovits, *Chem. Mater.*, 2000, **12**, 250.
- 42 D. Golberg, Y. Bando, K. Kurashima and T. Sato, *J. Nanosci. Nanotechnol.*, 2001, **1**, 49.
- 43 C. C. Tang, Y. Bando, D. Golberg, X. X. Ding and S. R. Qi, *J. Phys. Chem. B*, 2003, **107**, 6539.
- 44 R. Z. Ma, Y. Bando and T. Sato, *Chem. Phys. Lett.*, 2004, **350**, 1.
- 45 A. L. M. Reddy, B. K. Gupta, T. N. Narayanan, A. A. Martí, P. M. Ajayan and G. C. Walker, *J. Phys. Chem. C*, 2012, **116**, 12803.
- 46 P. C. P. Watts, W. K. Hsu, G. Z. Chen, D. J. Fray, H. W. Kroto and D. R. M. Walton, *J. Mater. Chem.*, 2001, **11**, 2482.
- 47 P. C. P. Watts, W. K. Hsu, D. P. Randall, V. Kotzeva and G. Z. Chen, *Chem. Mater.*, 2002, **14**, 4505.
- 48 K. Miyajima, A. Nakajima, S. Yabushita, M. B. Knickelbein and K. Kaya, *J. Am. Chem. Soc.*, 2004, **126**, 13202.
- 49 J. Wang, P. H. Acioli and J. Jelinek, *J. Am. Chem. Soc.*, 2005, **127**, 2812.
- 50 H. Xiang, J. Yang, J. G. Hou and Q. Zhu, *J. Am. Chem. Soc.*, 2006, **128**, 2310.
- 51 V. V. Maslyuk, A. Bagrets, V. Meded, A. Arnold, F. Evers, M. Brandbyge, T. Bredow and I. Mertig, *Phys. Rev. Lett.*, 2006, **97**, 097201.
- 52 M. Koleini, M. Paulsson and M. Brandbyge, *Phys. Rev. Lett.*, 2007, **98**, 197202.
- 53 K. Miyajima, M. B. Knickelbein and A. Nakajima, *Eur. Phys. J. D*, 2005, **34**, 177.
- 54 D. Rayane, A. R. Allouche, R. Antoine, M. Broyer, I. Compagnon and P. Dugourd, *Chem. Phys. Lett.*, 2003, **375**, 506.
- 55 K. Hoshino, T. Kurikawa, K. Takeda, A. Nakajima and K. Kaya, *J. Phys. Chem.*, 1995, **99**, 3053.
- 56 T. Kuhlmann, S. Roth, J. Rozière and W. Siebert, *Angew. Chem., Int. Ed.*, 1986, **25**, 105.
- 57 M. Y. Lavrentiev, H. Köppel and M. C. Böhm, *Chem. Phys.*, 1993, **169**, 85.
- 58 S. Nagao, A. Kato and A. Nakajima, *J. Am. Chem. Soc.*, 2000, **122**, 4221.
- 59 P. Kruse, E. R. Johnson, G. A. DiLabio and R. A. Wolkow, *Nano Lett.*, 2002, **2**, 807.
- 60 N. J. Long, *Metallocenes*, Blackwell Science Press, Oxford, 1998.
- 61 S. Nagao, A. Kato and A. Nakajima, *J. Am. Chem. Soc.*, 2000, **122**, 4221.
- 62 K. Miyajima, A. Nakajima, S. Yabushita, M. B. Knickelbein and K. Kaya, *J. Am. Chem. Soc.*, 2004, **126**, 13202.
- 63 J. Wang, H. P. Acioli and J. Jelinek, *J. Am. Chem. Soc.*, 2005, **127**, 2812.
- 64 V. M. Volodymyr, B. Alexei, B. Thomas and M. Ngrid, *Phys. Rev. Lett.*, 2006, **97**, 097201.
- 65 C. K. Yang, J. Zhao and J. P. Lu, *Phys. Rev. Lett.*, 2003, **90**, 257203.
- 66 E. Nakamura, M. Koshino, T. Saito, Y. Niimi, K. Suenaga and Y. Matsuo, *J. Am. Chem. Soc.*, 2011, **133**, 14151.



- 67 N. Sun, L. Guan, Z. Shi, N. Li, Z. Gu, Z. Zhu, M. Li and Y. Shao, *Anal. Chem.*, 2006, **78**, 6050.
- 68 G. Zhang, R. Zhou and X. C. Zeng, *J. Mater. Chem. C*, 2013, **1**, 4518.
- 69 G. Zhang, P. Sun, Y. Shang, Z.-D. Yang and X. C. Zeng, *J. Mater. Chem. C*, 2014, **2**, 10017.
- 70 J. Taylor, H. Guo and J. Wang, *Phys. Rev. B: Condens. Matter Mater. Phys.*, 2001, **63**, 245407.
- 71 M. Brandbyge, J. L. Mozos, P. Ordejón, J. Taylor and K. Stokbro, *Phys. Rev. B: Condens. Matter Mater. Phys.*, 2002, **65**, 165401.
- 72 J. M. Soler, E. Artacho, J. D. Gale, A. Garcia, J. Junquera, P. Ordejon and D. Sanchez-Portal, *J. Phys.: Condens. Matter*, 2002, **14**, 2745.
- 73 ATK, Version 13.8, atomistix a/s, 2013, www.quantumwise.com.
- 74 V. Volodymyr, A. B. Maslyuk, M. Velimir, A. Andreas, E. Ferdinand, B. Mads, B. Thomas and M. Ingrid, *Phys. Rev. Lett.*, 2006, **97**, 097201.
- 75 T. Yasuike and S. Yabushita, *J. Phys. Chem. A*, 1999, **103**, 4533.
- 76 R. Pandey, *et al.*, *Chem. Phys. Lett.*, 2000, **321**, 142.
- 77 I. Rungger and S. Sanvito, *Phys. Rev. B: Condens. Matter Mater. Phys.*, 2008, **78**, 035407.
- 78 V. V. Maslyuk, A. Bagrets, V. Meded, A. Arnold, F. Evers, M. Brandbyge, T. Bredow and I. Mertig, *Phys. Rev. Lett.*, 2006, **97**, 097201.

